



Dynamic behavior of CrMnFeCoNi high-entropy alloy in impact tension

Yu Qiao^{a,b,c}, Yan Chen^{b,c,*}, Fu-Hua Cao^{b,c}, Hai-Ying Wang^{b,c}, Lan-Hong Dai^{a,b,c,d,*}

^a CAS Key Laboratory of Mechanical Behavior and Design of Materials, Department of Modern Mechanics, University of Science and Technology of China, Hefei, 230027, China

^b State Key Laboratory of Nonlinear Mechanics, Institute of Mechanics, Chinese Academy of Sciences, Beijing, 100190, China

^c School of Engineering Science, University of Chinese Academy of Sciences, Beijing, 101408, China

^d State Key Laboratory of Explosion Science and Technology, Beijing Institute of Technology, Beijing, 100081, China

ARTICLE INFO

Keywords:

High-entropy alloy
Split Hopkinson tensile bar
Strain rate effect
Dislocation
Twin

ABSTRACT

High-entropy alloys (HEAs), recently emerging alloy materials with numerous excellent performances, may have a wide application prospect in impact engineering. However, previous research regarding the mechanical behavior of HEAs has primarily focused on quasi-static testing, whereas the dynamic mechanical behavior of HEAs at high strain rates remains elusive. In this paper, the unusual simultaneous strength-plasticity enhancement and the inhibition of the high strain rate embrittlement of CrMnFeCoNi HEA in impact tension were revealed via split Hopkinson tensile bar (SHTB) with high-speed photography. Quantitative microstructural analysis indicates that the cooperation of twins and dislocations is the crucial mechanism for the synchronous enhancement of strength-plasticity in this alloy under impact tension. A thermo-viscoplastic constitutive model based on dislocations and twins evolution was developed to describe dynamic mechanical behavior. The high plastic hardening under dynamic tension was revealed to be induced by high dislocation forest hardening and strong resistance of twins to dislocation motion. The excellent combination of dynamic strength-plasticity of CrMnFeCoNi HEA makes it becoming a promising candidate for impact engineering applications.

1. Introduction

The service safety of structural and alloys under high strain rate loadings has always been a key issue in aerospace, civil transportation, the defense industry, and other engineering applications [1–10]. The service conditions of impact engineering have stringent requirements on the strength, plasticity, and toughness of materials [2,4]. Considerable studies have been carried out on the dynamic mechanical behavior of traditional single-principal element alloys under impulsive loadings [11–16]. One critical problem is the plasticity or ductility degradation of metallic materials subjected to high strain rate loadings, i.e., high strain rate embrittlement. The high strain rate embrittlement presents a severe challenge to the service safety of metallic materials under impulsive loadings. Several new structures and materials have emerged in recent years, and their potential application in impact engineering has raised a keen research interest [17–21]. Among these, the multiple-principal element high entropy alloy (HEA), as a new chemically-disordered alloy, is one of the most promising materials owing to its excellent combination of strength and plasticity even under dynamic loadings.

HEAs are a unique class of alloys with a high mixing entropy and a

near-equiatomic ratio [22–28]. Their topologically-ordered lattice structure with randomly arranged multi-element atoms imparts many fascinating properties to the HEAs, including excellent combination of strength and ductility [29–32], outstanding cryogenic plasticity [33], good hydrogen embrittlement resistance [34], and exceptional “self-sharpening” capability [35]. Many of these properties signify that these new HEAs have great potential in impact engineering. However, previous studies on the mechanical behavior of HEAs have mainly focused on the quasi-static state. As for dynamic behavior, Dai and co-workers reported the shock response of two typical equiatomic HEAs for the first time in 2016 and revealed that these two kinds of HEA exhibit relatively high Hugoniot elastic limit and high-phase transition threshold stress [36]. Subsequently, a few studies on dynamic tensile, compression, and shear behaviors have been reported in recent years [37–45]. However, the precise picture of the strain rate-dependent microstructure evolution and its link with macroscopic mechanical behavior remains elusive. As the most typical HEA, the Cantor alloy (i.e., CrMnFeCoNi) has been proven to be a single FCC solid solution alloy (FCC: face-centered cubic) [27]. In recent years, the strain rate and temperature related mechanical behavior of the CrMnFeCoNi HEA has received extensive attention from

* Corresponding authors:

E-mail addresses: chenyan@lnm.imech.ac.cn (Y. Chen), lhdai@lnm.imech.ac.cn (L.-H. Dai).

<https://doi.org/10.1016/j.ijimpeng.2021.104008>

Received 2 January 2021; Received in revised form 8 July 2021; Accepted 10 August 2021

Available online 18 August 2021

0734-743X/© 2021 Elsevier Ltd. All rights reserved.

researchers, including adiabatic shear localization [37,46], strain rate sensitivity [47,48], low-temperature serrated flow [33,49]. Moreover, deformation twins are common microstructural mechanisms of this HEA under extreme loading conditions such as low temperature or shock [34, 36]. However, the unabridged dynamic tensile behavior of the CrMnFeCoNi HEA and especially the influence of twins on the plastic flow behavior are still unknown.

In this work, we selected the stable single-phase FCC alloy, CrMnFeCoNi HEA, for quasi-static and dynamic mechanical experiments. A split Hopkinson tensile bar (SHTB) device paired with high-speed photography was used for dynamic tensile testing of the HEA. The evolution of the dislocations and twins was discussed by observing multiscale microstructural morphology. Electron backscatter diffraction (EBSD) experiments measured the quantized dislocation density and twin integration number. Finally, a thermo-viscoplastic constitutive model based on the evolution of the alloy microstructure was established to describe the hardening mechanism of the strain rate-dependent mechanical behavior.

2. Material and methods

2.1. Alloy preparation

The equiatomic CrMnFeCoNi HEA used in this work was prepared by arc smelting the high-purity metal mixture (purity of each component > 99.9 wt%) in a high-purity argon environment. The ingot was repeatedly smelted at least five times to ensure the chemical uniformity of the alloy. After smelting, the initial ingot was cut into 7 mm-thick plates and then cold rolled with 70% reduction to 2.1 mm-thick sheets. The sheets were then placed in an annealing furnace and heated for 90 min to 820 °C, and then held at this temperature for 60 min to fully recrystallize. Subsequently, the sheets were naturally cooled to room temperature in the furnace, whereupon the alloy sheets with an average grain size of 6.83 μm were obtained (Fig. 1(a) and 1(b)). The specimens were basically composed of randomly oriented equiaxed grains. The 'dog bone' tensile specimens were cut from the recrystallized sheets by wire electrical discharge machining, where the tensile direction of the specimens was consistent with the rolling direction of the sheets. The test section sizes of the quasi-static and dynamic tensile specimens were 3.8 mm \times 2 mm \times 12 mm and 3.8 mm \times 1 mm \times 2 mm (width \times thickness \times length), respectively. Moreover, the arc transition section diameters of the quasi-static and dynamic 'dog bone' specimens were 4 and 0.5 mm, respectively. The surfaces of all specimens were polished with 2000-grit SiC papers.

2.2. Quasi-static and dynamic tensile testing

The quasi-static tensile tests (strain rate $\dot{\epsilon} = 5 \times 10^{-4} \text{ s}^{-1}$) were performed on a material testing machine (UTM4204), where an extensometer measured the strain data of specimens. In the dynamic tensile tests, the SHTB with a diameter of 12 mm was used, whose detailed schematic diagram is shown in Fig. 2(a). In the SHTB, the length of the sleeve striker was 400 mm, and the bars and sleeve striker were made of steel with Young's modulus of 210 GPa and a density of $7.8 \text{ g}\cdot\text{cm}^{-3}$. In each dynamic test, two 1mm thick quarter-ring rubber sheets were used as the shapers. The specimens were affixed to special chucks using structural glue (ergo1309), and the special chucks were threaded on the bars to ensure connection. Fig. 2(b) shows a typical original waveform. The stress-strain curves were calculated by the double-wave method in this work [50]. The strain rate for dynamic testing was approximately 7000 s^{-1} . As a consequence of the small length ratio of only 4 between the test section length and the arc transition section radius of the dynamic test specimens, the deformation of the arc transition section was nonnegligible when calculating the strain. To correct the error caused by the deformation of the arc transition section, the parameter l_m was introduced as the modified test section length [51], such that

$$l_m = l_0 + \sqrt{R \frac{b_0(\sigma_{\max} - \sigma_y)}{\sigma_y} - \frac{b_0^2(\sigma_{\max} - \sigma_y)^2}{\sigma_y^2}}, \quad (1)$$

where l_0 and b_0 are the initial length and width of the test section, respectively; R is the radius of the arc transition section; and σ_y and σ_{\max} are the yield and ultimate stress, respectively. When calculating the strain of the dynamic test, the stress curves of the specimens were first calculated. The yield stress σ_y and ultimate stress σ_{\max} were substituted into Eq. (1) to calculate the modified test section length l_m . Finally, l_m was used to calculate the accurate strain of the dynamic test.

In the dynamic test, a high-speed camera (FASTCAM SA-X) with a shutter speed of 100,000 fps was used to observe the deformation process of the specimens and thus confirm whether the specimen breaks under the first load wave. To enable strain field measurements, the tensile specimens were painted with a speckle pattern prior to testing. Finally, the captured videos were processed using GOM Correlate 2019 software for digital image correlation (DIC) analysis to calculate the strain field on the specimen surface.

2.3. Microstructural characterization

Microscopic characterization methods for the quasi-static and dynamic tensile specimens included scanning electron microscopy (SEM);

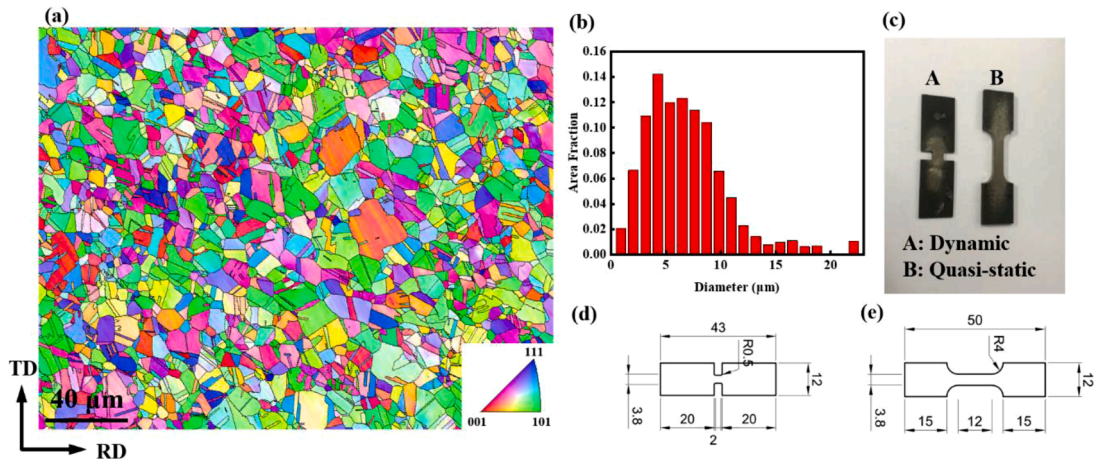


Fig. 1. (a) EBSD IPF map of the recrystallized CrMnFeCoNi HEA microstructure, (b) histogram of statistical grain size, (c) photographs of the quasi-static and dynamic tensile specimens, and (d, e) detailed dimensions of the (d) dynamic and (e) quasi-static specimens (units in mm).

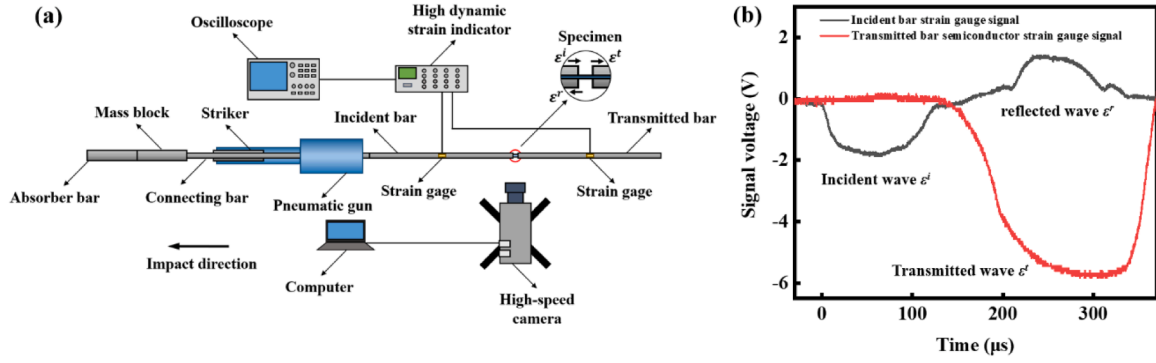


Fig. 2. (a) Schematic diagram of the SHTB device; (b) typical original waveform.

JSM-7900F), electron backscattered diffraction (EBSD), and transmission electron microscopy (TEM; JEM-2100F). The SEM experiments observed the microscopic morphology of the specimen fracture, whereas the EBSD and TEM experiments observed the specimen's microstructural evolution after plastic deformation. The specimens used for TEM observation were obtained by focused ion beam (FIB) processing, and the observation conditions and parameters of the microstructural characterization are described in detail in Section 3.3.

3. Results and discussion

3.1. Stress-strain relationship

During dynamic testing with a strain rate of less than 5000 s^{-1} , the first tensile wave of SHTB is challenging to break the specimens. Incomplete loading is caused by the remarkable plasticity of the CrMnFeCoNi HEA and the insufficient loading tension of the 12 mm SHTB device used in this work. Therefore, to ensure the integrity of the stress-strain curves, a strain rate of 7000 s^{-1} was chosen for the dynamic tensile testing in this work. Fig. 3 shows the engineering (Fig. 3(a)) and true (Fig. 3(b)) stress-strain curves of the CrMnFeCoNi HEA. Under quasi-static tension, the yield strength of the CrMnFeCoNi HEA is 399 MPa, whereas the true ultimate tensile stress and strain under quasi-static conditions are 1042 MPa and 0.34, respectively. The increased load strain rate from quasi-static ($5 \times 10^{-4} \text{ s}^{-1}$) to dynamic (7000 s^{-1}) induced an 18% increase in the yield strength (472 MPa), a 52% increase in the true ultimate tensile stress (1586 MPa), and a 68% increase in the true ultimate tensile strain (0.57). Comparing the tensile test results of these two strain rates, the CrMnFeCoNi HEA exhibited a higher work hardening at high strain rates, and both the strength and plasticity of the CrMnFeCoNi HEA were enhanced significantly at high strain rates.

3.2. Dynamic deformation and fracture behavior

The deformation process of the dynamic tensile specimens was recorded in situ by high-speed photography. The specimen surface observed by the high-speed camera is shown in Fig. 4(a), from which the true strain fields of the specimen surface were calculated by the DIC method (the strain mentioned in Section 3.2 are true strain). In Fig. 4(a), the areas of the specimens test section and the DIC calculation are marked in yellow and red rectangles, respectively. Fig. 4(b) includes the relevant high-speed photographs and DIC results of the dynamic specimens marked on the stress-strain curve. The duration of a single dynamic tensile experiment is approximately 150 μs , and the high-speed photographs indicate that the specimen deformation process is basically divided into three stages. First, a uniform deformation stage occurs prior to the strain reaching 0.25 (approximately 0–90 μs). Second, a strain concentration appears in the middle of the specimens at a strain range of 0.25–0.46 (approximately 90–130 μs). Third, the specimens begin to shrink until fracture. The above deformation process indicates that the studied HEA has excellent deformation uniformity and that the deformation localization phenomenon appears late in the process. Fig. 4(c) shows the strain-time curves of the dynamic tensile specimens obtained by DIC calculation and SHTB experiment. The consistency between the two curves indicates that the experiments in this work are accurate. To further analyze the strain distribution on the specimen surface, an expanded area including all test sections and a portion of the arc transition sections were selected for DIC calculation (marked in blue in Fig. 4(a)). The calculated strain field of this expanded area was divided into 30 equal parts along the x-direction, whereupon the average strain value and standard deviation of each part were calculated. Finally, the strain distribution curves (including error bars) at 0, 60, 90, 110, 130, and 150 μs after dynamic loading are shown in Fig. 5 (a). The deformation law of the specimens reflected by the strain

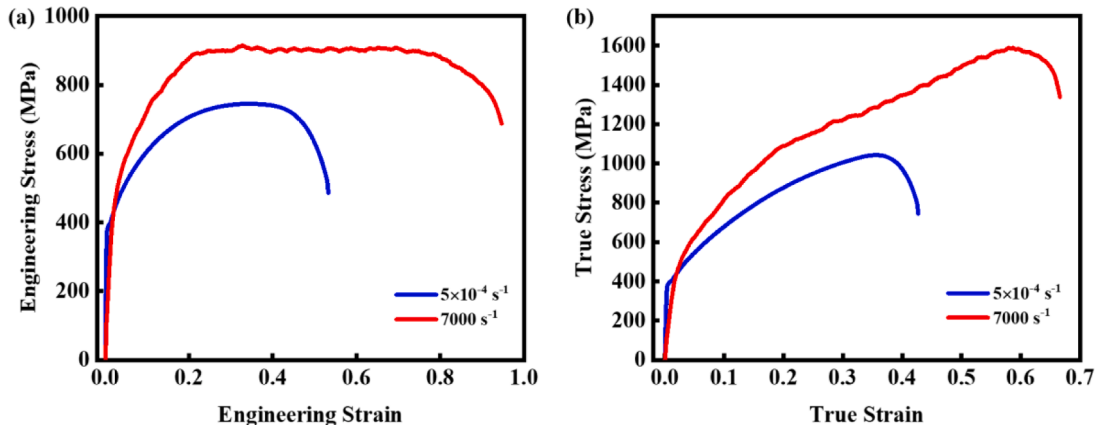


Fig. 3. (a) The engineering and (b) the true stress-strain curves of the CrMnFeCoNi HEA in different strain rates of $5 \times 10^{-4} \text{ s}^{-1}$ and 7000 s^{-1} .

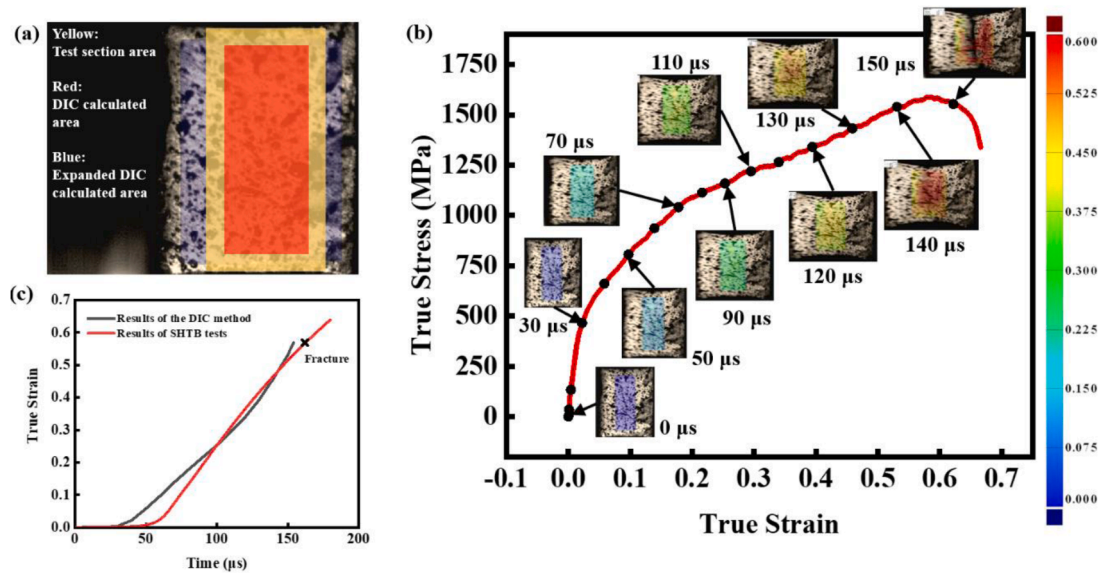


Fig. 4. (a) High-speed photography field-of-view and schematic diagrams of DIC calculation areas; (b) high-speed photographs correlated to a stress-strain curve of the CrMnFeCoNi HEA under dynamic tension; (c) strain-time curves obtained by the DIC method (black) and SHTB experimental tests (red). (For interpretation of the references to color in this figure legend, the reader is referred to the web version of this article.)

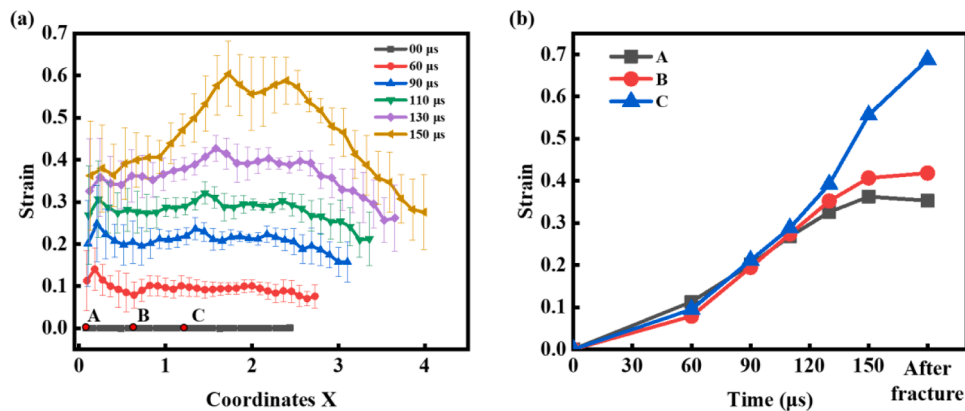


Fig. 5. (a) Strain distribution curves including error bars along the x-direction at 0, 60, 90, 110, 130, and 150 μs after dynamic tension; (b) strain-time curves of points A, B, and C on the expanded DIC calculation area (red labeled dots on (a)). (For interpretation of the references to color in this figure legend, the reader is referred to the web version of this article.)

distribution curve is consistent with the high-speed photographs. Note that the strain values (0.2–0.3) in the transition arc section of the specimen are relatively low. Fig. 5(b) plots the strain-time curves for three positions A–C selected from the expanded DIC calculation area, where the points A, B, and C are located at the edge, quarter, and center of the expanded DIC calculation area. For the times prior to 110 μs (the average strain is 0.31), the strains of the three positions are basically the same, where the smaller strain values at the specimen edge are owing to the earlier cessation of the deformation process. This result indicates that the strain rate of each position on the specimen surface is basically the same during most of the deformation process. In Section 3.3, the observation and analysis of the microstructures of the small strain regions in the dynamic tensile specimens are detailed.

After tensile testing, the fractured specimens were collected for fracture surface observation by SEM experiment. Fig. 6 shows the microscopic morphology of the specimen fractures after quasi-static and dynamic tensile failure. As shown in Fig. 6(a) and 6(c), dimples are the main feature of quasi-static tensile specimen fracture, with a large number of orthogonal dimples and some shear dimples occurring on the fracture surface. This fracture indicates that CrMnFeCoNi HEA is a

typical ductile fracture under quasi-static tension. However, multiple fracture characteristics are found in dynamic tensile specimens. The dimple fracture of the dynamic tensile specimen fracture is similar to that of the quasi-static tensile specimens and remains the dominant fracture characteristic. Furthermore, quasi-cleavage fracture characterized by tearing dimples, river patterns, and tearing ridges is observed on the dynamic tensile specimens. The dimples and quasi-cleavage fractures are staggered on the dynamic tensile specimens, with clear boundaries between these two fracture types (Fig. 6(d–f)). Dimples are the primary feature of polycrystalline metals in ductile fracture [52], whereas quasi-cleavage fracture is a mode between cleavage and dimple fracture, suggesting a transition from ductile to brittle [53]. In previous reports regarding HEAs, the Al₃CrMnFeCoNi HEA has been reported to transform from ductile fracture to quasi-cleavage fracture, characterized by river patterns and tear ridges the influence of the BCC phase and a high strain rate [42]. However, Fig. 6(e) shows that a large dimple fracture area still exists on the dynamic tensile sample fracture. Therefore, the high strain rate embrittlement effect of CrMnFeCoNi high-entropy alloy is suppressed.

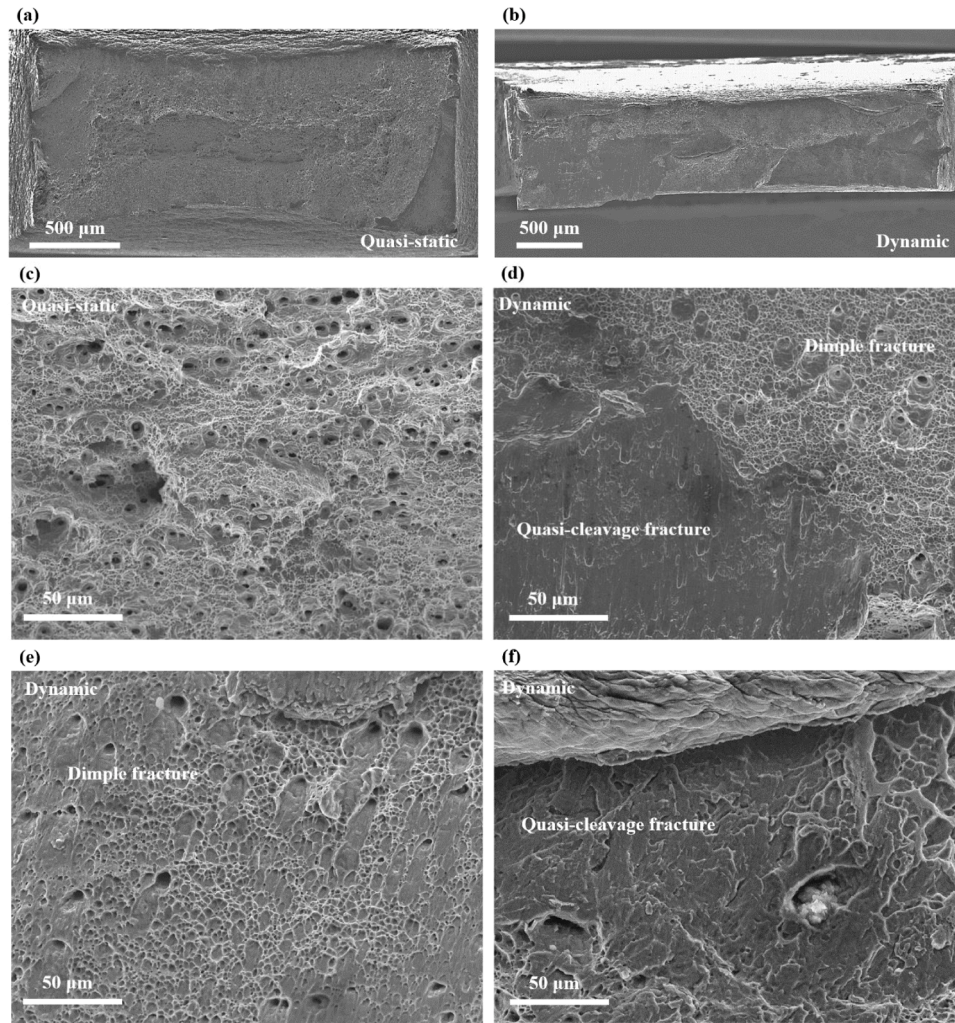


Fig. 6. SEM images of the specimen fracture morphology under quasi-static (strain rate $5 \times 10^{-4} \text{ s}^{-1}$) and dynamic (strain rate 7000 s^{-1}) tension; (a) quasi-static fracture, (b) dynamic fracture, (c) dimples of quasi-static fracture, (d, e, f) dimple and quasi-cleavage fracture of dynamic tensile specimens.

3.3. Strain rate-dependent microstructural evolution

To further explore the deformation mechanism of the CrMnFeCoNi HEA under dynamic tension at the sub-micrometer level under dynamic tension, EBSD measurements ($0.2 \mu\text{m}$ step size) were obtained of the undeformed, quasi-static, and dynamic fracture specimens. Fig. 7(a–c) shows the x-direction IPF (IPF_x) maps of these three specimen types, respectively, which coincides with the rolling direction (RD). Compared with the equiaxed grains of the undeformed specimens, the grains of the deformed specimens exhibit significant twisting and stretching along the tensile direction. The degree of grain torsion and tension of the dynamic tensile specimens are particularly severe due to the high-stress state and the significant plastic deformation of the alloy under dynamic tension. On the other hand, there are some annealing twins in the undeformed samples, and the effect of annealing twins on the mechanical properties of the materials is not discussed in this paper. We excluded all annealing twins in the subsequent analysis. According to the large width of annealing twin (micron-sized) and the characteristics of straight twin boundary, it is easy to distinguish from nano deformation twins. The twins in the following context generally represent nano deformation twins formed during the plastic deformation of HEAs. Deformation twins are scarcely observed in the quasi-static tensile specimens, whereas many deformation twins are observed in the dynamic tensile specimens. To quantify the number of deformation twins in the specimens, we obtained image quality (IQ) maps of the undeformed, quasi-static, and

dynamic tensile specimens (Fig. 7(d–f), respectively), wherein the deformation twin boundaries are marked with red lines. The size of the nanotwinning bundle of deformation twins (about $10\text{--}200 \text{ nm}$) is much smaller than the observed range of EBSD experiments (about $80 \mu\text{m}$). In order to count deformation twins, we divide the number of pixels identified by the analysis software as twins by the total number of pixels scanned to obtain the twin volume fractions (the scanning step size is 200 nm) [54]. It is evident that only a few deformation twins are present on the quasi-static tensile specimens, and the twin volume fraction of the quasi-static tensile specimen was estimated as 0.004. Conversely, some grains were observed to be densely packed with deformed twin lamellas on the dynamic tensile specimens, and the twin volume fraction was estimated as 0.021. We note that the twin volume fraction measured in the studied CrMnFeCoNi HEA dynamic tensile specimen is lower than that obtained with low-temperature loading conditions or HEAs comprising other elements [30,41]. This result may be owing to the relatively higher stacking fault (SF) energy of the CrMnFeCoNi HEA at room temperature. Kernel average misorientation (KAM) maps are an analysis method that directly reflects the distribution of defects and plastic deformation within an alloy and allows an estimate of their dislocation density [55]. Fig. 7(g–i) respectively show the KAM maps of the undeformed, quasi-static, and dynamic tensile specimens, where all KAM maps were drawn with the first nearest neighbor, and the maximum misorientation angle was 5° . In the KAM map, the color bar ranging from blue to red corresponds to KAM values ranging from 0° to

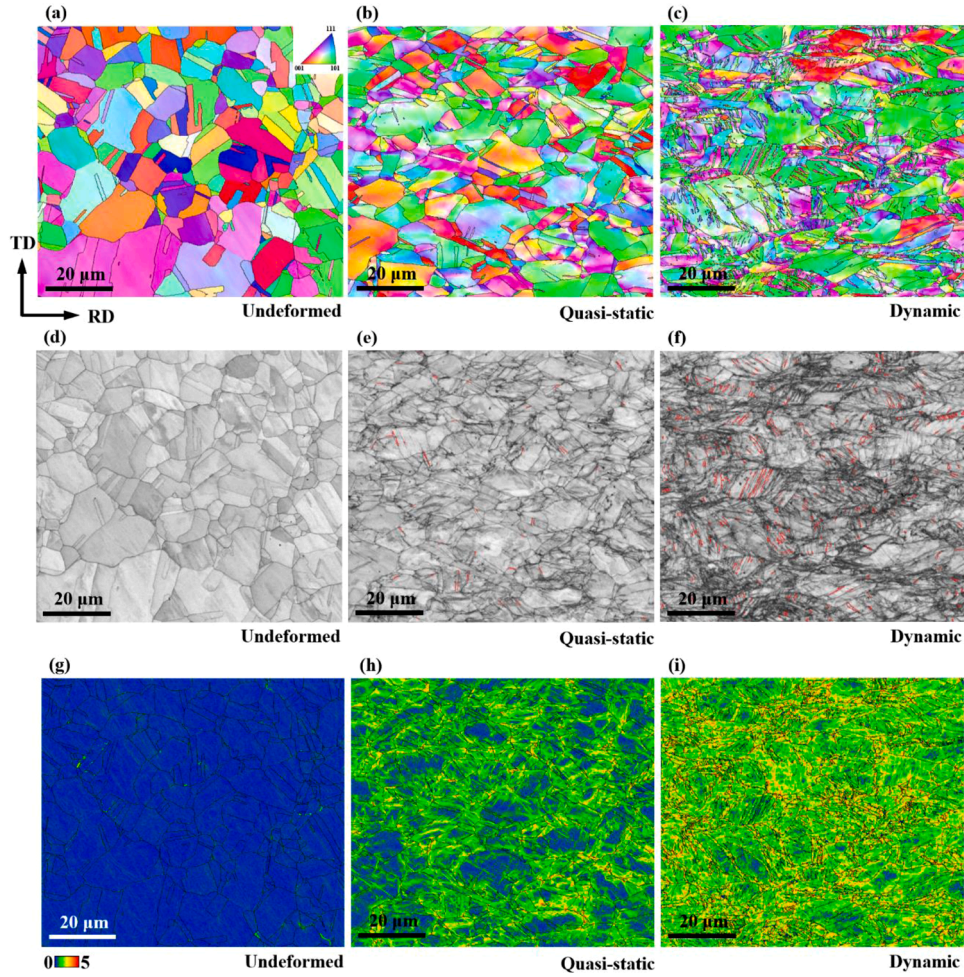


Fig. 7. Microstructural analysis of the undeformed, quasi-static (strain 0.34, strain rate $5 \times 10^{-4} \text{ s}^{-1}$) and dynamic (strain 0.57, strain rate 7000 s^{-1}) tensile CrMnFeCoNi HEA specimens via EBSD: (a–c) IPF map; (d–f) IQ map with twin boundary labeling (red lines); (g–i) KAM maps. (For interpretation of the references to color in this figure legend, the reader is referred to the web version of this article.)

5° (bottom of Fig. 7(g)), and the black lines in the maps represent grain boundaries. The KAM map of the undeformed specimen is primarily a deep blue color, indicating that the KAM values of most areas in this sample were close to 0° . It means that the dislocations and defects in the undeformed alloy are few and evenly distributed. The KAM map of the quasi-static specimen exhibit that most areas turned a green color after plastic deformation. The number of dislocations increases appreciably after plastic deformation. Furthermore, the KAM values at the grain boundaries and small grains are more prominent, signifying concentrations of dislocations and other defects at these locations. The KAM map of the dynamic tensile specimens shows more dislocation enrichment at the grain boundaries and small grains. Excepting the center of some large grains, there is a considerable accumulation of dislocations. To quantify the dislocation density in the specimens [56], The dislocation density was calculated by the following formula:

$$\rho = \frac{2\theta_{\text{KAM}}}{\mu b}, \quad (2)$$

where ρ is the dislocation density, b is the Burgers vector, and $\mu = nd$ is the kernel size (where n is the defined nearest neighbor and d is the scan step). The estimated dislocation densities of undeformed, quasi-static, and dynamic tensile specimens are calculated as 2.60×10^{13} , 7.62×10^{14} , and $1.19 \times 10^{15} \text{ m}^{-2}$, respectively. The above results indicate that the dislocation motion resistance enhancement of the CrMnFeCoNi HEA increases flow stress the as a result of the strain rate effect. However, high dislocation motion resistance has a negative effect on material

plasticity. For example, 316L stainless steel exhibits increased strength but reduced plasticity under dynamic loading [42]. Therefore, the fracture surface of the CrMnFeCoNi HEA exhibits a tendency to change from tough to brittle locally. Additionally, similar to the effect on the CrMnFeCoNi HEA under a low-temperature environment, more deformation twins are nucleated and develop under dynamic tension. It has been previously demonstrated that twins increase the capacity of a material to store dislocations [31]. Furthermore, twins aid the formation of deep dimples during the fracture process, which effectively resists the nucleation and propagation of cracks [43, 44].

As mentioned in Section 3.2, the microstructure of dynamic tensile specimens under varying strain can be analyzed. According to the strain field distribution calculated by the expanded DIC (Fig. 5(a)), the microstructures of three different strain positions on the dynamic tensile specimens were observed. Fig. 8 shows a series of EBSD results for a dynamic tensile specimen under strains of 0.26, 0.46, and 0.57, where Fig. 8(a–c) shows the IPF maps of the specimens with varying strains along the RD, respectively. For the strain of 0.26, the degree of grain deformation is low, the grains remain equiaxed, and the nucleation of deformation twins is observed in individual grains. When the strain of the dynamic tensile specimen increases to 0.46, the grain exhibits a distinct twist and stretch along the tensile direction, and the orientation difference between some grains is significantly increased. Moreover, the nucleated deformation twins exhibit further development, and dense deformation twin lamellas have evolved in some grains. Ultimately, when the specimen deforms to strain 0.57, many grains exist with

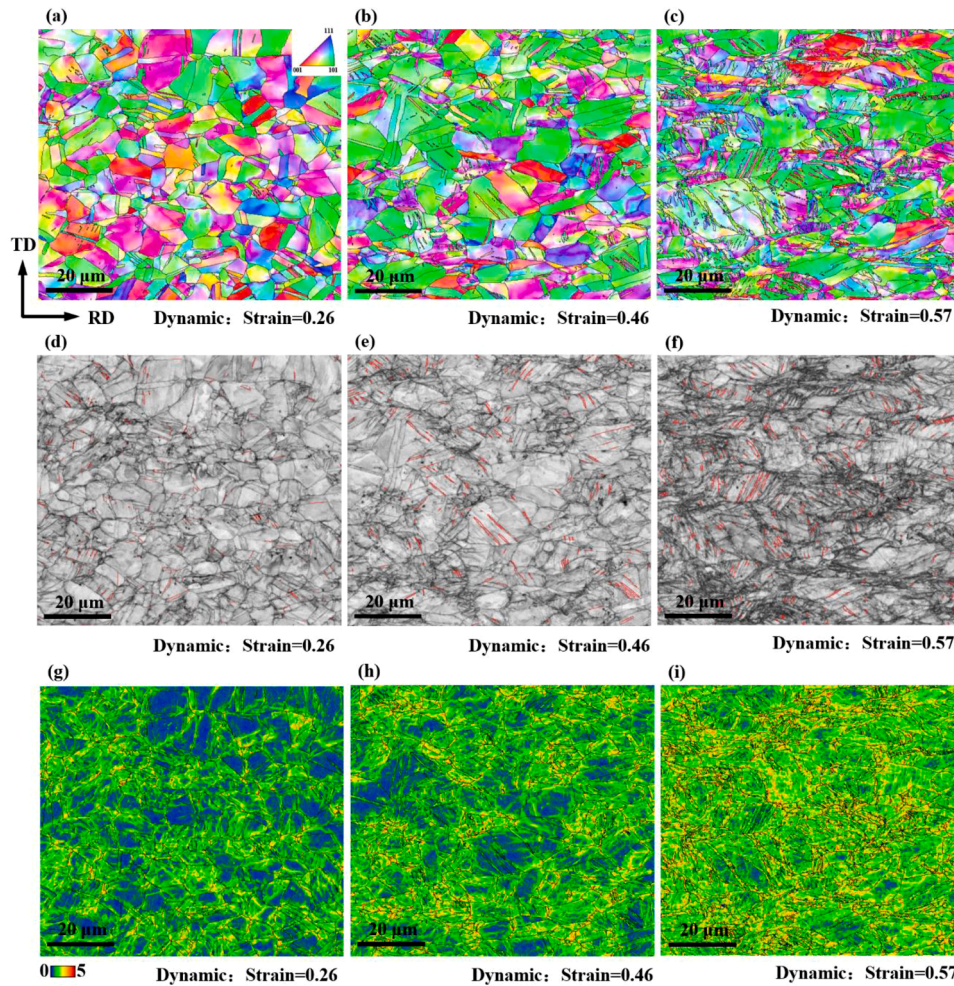


Fig. 8. Microstructural analysis via EBSD of the dynamic (strain rate 7000 s^{-1}) tensile CrMnFeCoNi HEA specimen with strain values of (a, d, g) 0.26, (b, e, h) 0.46, and (c, f, i) 0.57: (a–c) IPFx map; (d–f) IQ map with twin boundary labeling (red lines); (g–i) KAM maps. (For interpretation of the references to color in this figure legend, the reader is referred to the web version of this article.)

violent torsion and tension and a considerable number of deformation twins. Fig. 8(d–f) indicates a twin volume fraction of 0.006 and 0.015 for the dynamic tensile specimens with strains of 0.26 and 0.46, respectively. Fig. 8(g–i) shows KAM maps of the evolution of the dynamic tensile specimens with varying strain. Similar to Fig. 7(h), Under finite plastic deformation, the high KAM values are primarily distributed in the fine grain regions, grain boundaries, and few grains. When the strain of the dynamic tensile specimen increases to 0.46, more large grains begin to exhibit a sharp increase in KAM values. This result signifies a rapid accumulation of dislocations in the grains. Finally, the dynamic tensile specimen indicates that most of the grains have high KAM values at a strain of 0.57, indicating a considerable accumulation of dislocations in the grains at this time. The KAM map at this point is almost entirely covered in green. Furthermore, using Eq. (2), the dislocation densities of the dynamic tensile specimens with strains of 0.26 and 0.46 were estimated as 7.55×10^{14} and $9.07 \times 10^{14} \text{ m}^{-2}$, respectively.

It has been observed that the primary deformation mechanisms of CrMnFeCoNi HEA are dislocations and twins. In particular, the presence of twins is crucial for simultaneous strength and plasticity enhancement of HEAs at high strain rates. To observe the microstructure of the deformed CrMnFeCoNi HEA specimens at the nanoscale, the quasi-static and strain dynamic tensile specimens with the strain of 0.34 and 0.57 were cut using the FIB method to prepare the specimens for TEM observation. The TEM bright-field images revealing the quasi-static and dynamic tensile specimen dislocation morphology are shown in Fig. 9(a) and 9(b), respectively. The magnifications of Fig. 9(a) and 9(b) are

consistent. The observation conditions under which the micrographs were obtained feature the same double-beam condition ($g = (111)$) (indicated with black arrows in Fig. 9). Fig. 9(a) reveals the presence of some dislocation cells (DCs) and tangles on the quasi-static tensile specimen, which have been similarly observed in some previous reports [30,41]. During severe deformation, the high-density dislocation accumulation reassembles into DCs, thereby refining coarse/fine grains to form nanograins [57]. In the dynamic tensile specimens shown in Fig. 9 (b), the higher density of dislocation clusters and DCs was observed, and the DC size on the dynamic tensile specimen is generally smaller than that on the quasi-static tensile specimens. It has been reported that the average DC diameter can be considered inversely proportional to the root of the dislocation density [58]. Furthermore, the smaller DC size in the dynamic tensile specimen provides the alloy with higher flow stress. Thus, the high dislocation density is the key to the flow stress strengthening of the CrMnFeCoNi HEA under dynamic loading. However, the high dislocation density typically limits the movement of dislocations and induces the formation of accumulations, which leads to a strength-ductility trade-off dilemma at high strain rates [59,60]. On the other hand, the twin boundaries strengthen the alloy by blocking the movement of dislocations without a significant sacrifice of plasticity. In our work and other reports, for a CrMnFeCoNi HEA under dynamic or low-temperature loading conditions, the dense twin boundaries simultaneously enhance the strength and plasticity of the alloy [30,34].

Fig. 10 shows TEM micrographs of the twin and SFs morphology. Fig. 10(a) and 10(b) show TEM bright-field images revealing typical

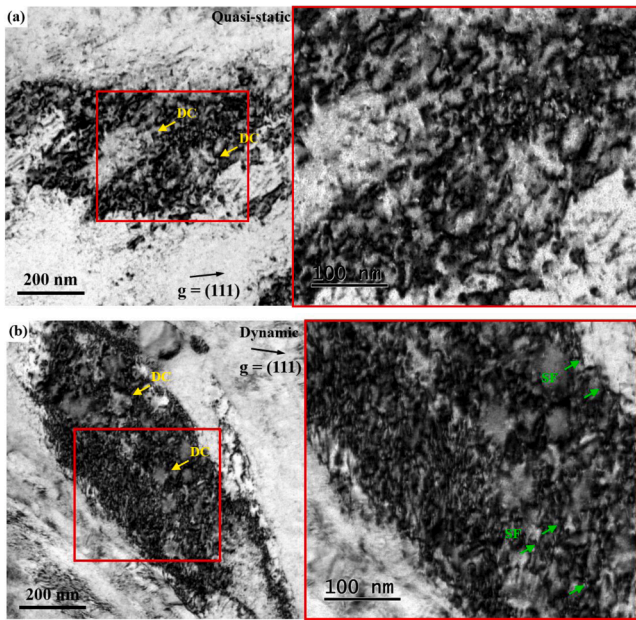


Fig. 9. Bright-field TEM images revealing the dislocation morphology of the (a) quasi-static and (b) dynamic tensile specimens. Enlarged image (right side) of the red frame area indicated on the left side. Indicated in each image are the double-beam condition (g ; black arrows), dislocation cells (DC; yellow arrows) and stacking faults (SF; green arrows). (For interpretation of the references to color in this figure legend, the reader is referred to the web version of this article.)

twin morphologies within the quasi-static and dynamic tensile specimens, respectively. Deformation twins were observed in both the quasi-static and dynamic tensile specimens, and selected area diffraction (SAD) patterns obtained near the twins all reveal two sets of diffraction spots belonging to the FCC twins and the FCC matrix. Deformation twin

lamellas on the quasi-static tensile specimen are sparse and scattered, whereas a large number of close-packed deformation twins are observed in some grains of the dynamic tensile specimens. Deformation twins generally are observed in alloys possessing moderate/low SF energy after large plastic deformation, which is the deformation mechanism that increases material strength and plasticity. Moreover, Fig. 10(c) reveals many SFs around the deformation twins, whereas a high-resolution TEM image in the lower-left corner of Fig. 10(c) shows a clear twin boundary. Furthermore, the SAD patterns near the SFs (upper-right corner of Fig. 10(c)) indicate the spreading of FCC spots into streaks. It is generally believed that SFs are the precursors of twins. In another report on CoCrFeNiNb_{0.1} HEA specimens, only some SFs were observed in the sample when cold rolled to 10% at low temperature, whereas nanotwins were generally observed in the specimen when cold rolled to 25% at low temperature [61]. Fig. 10(d) shows a high-resolution TEM image of the deformation twins present in the dynamic tensile specimens, where the twin boundaries are marked with solid yellow lines in the image. The observation of SFs (green arrows in Fig. 10(d)) was common around the twin boundary steps, which may be related to the formation and evolution of the twin boundaries. In particular, some continuous SF lines (dashed green lines in Fig. 10(d)) were observed in the high-resolution TEM image. We also note the nucleation of a new twin boundary (solid yellow lines in Fig. 10(d)) when three consecutive layers of atoms manifest SFs. Moreover, Fig. 10(d) reveals the repeatedly interrupted twin boundary steps in the dynamic tensile specimen subjected to severe plastic deformation. This phenomenon may be the trace of the interaction between twin boundaries and dislocations. There is currently a possible explanation for the positive effect of twins on alloy plasticity: First, a possible situation explaining the interaction between dislocations and twin boundaries is the decomposition of dislocation into a partial dislocation that moves over the twin boundary and a partial dislocation that remains on the twin boundary. The latter partial dislocation is absorbed by the twin boundary, inducing the twin boundary to migrate and form a step. This process effectively releases the stress concentration caused by the deformation, signifying that the twin boundary has the ability to accommodate considerable plastic

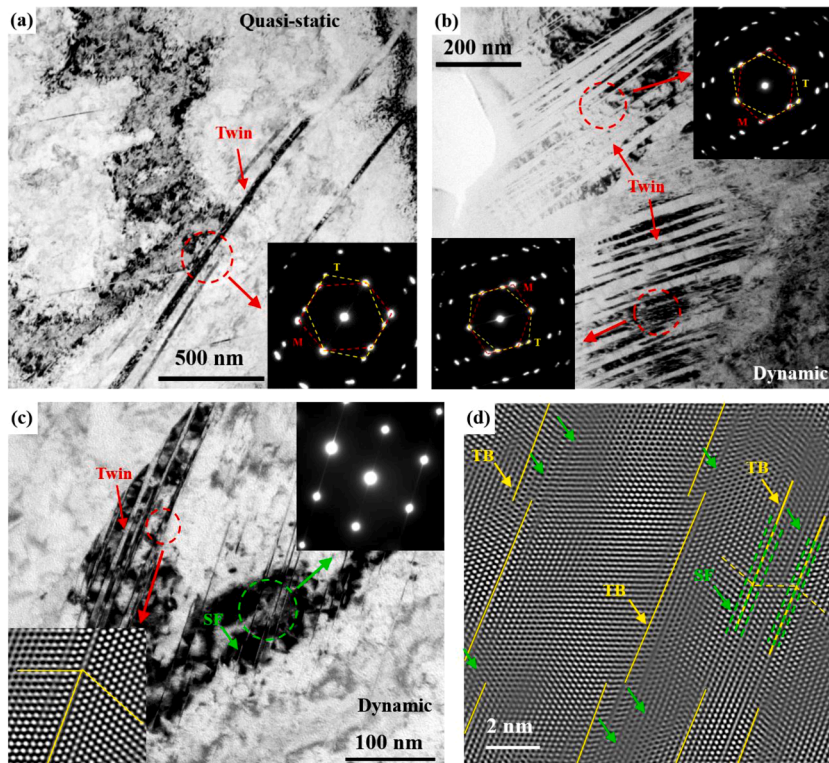


Fig. 10. Bright-field TEM micrographs revealing twins and SFs: (a) quasi-static tensile specimen showing typical twin morphology; (b–d) dynamic tensile specimen showing (b) typical twin morphology, (c) twin/SF morphology, and (d) high-resolution TEM image of twin/SF. Indicated in each image are the twins (red arrows), twin boundaries (TB; yellow arrows/lines) and stacking faults (SF; green arrows/lines). (Insets) SAD patterns from corresponding sample areas in the dashed circle. (For interpretation of the references to color in this figure legend, the reader is referred to the web version of this article.)

strain [62–64]. Therefore, the cooperation of twins and dislocations is crucial for the synchronous enhancement of strength and plasticity in this alloy under dynamic tension.

4. Constitutive model based on dislocation and twin evolution

The observations and analysis of microstructure given in Section 3.3 reveal and quantify many dislocations and twins in the CrMnFeCoNi HEA specimens under dynamic tension. Consequently, a thermoviscoplastic constitutive model that independently considers this twin enhancement effect is introduced, and is summarized as

$$\sigma_{flow}(\epsilon_p, \dot{\epsilon}, T) = \sigma_{matrix} + \sigma_{twin}, \quad (3)$$

where σ_{flow} is the flow stress related to the plastic strain ϵ_p , the strain rate $\dot{\epsilon}$, and the temperature T ; σ_{matrix} is the matrix-related stress; and σ_{twin} is the twin-related stress. The stresses of the CrMnFeCoNi HEA matrix and the twins as weighting by their content in the alloys are given as

$$\sigma_{flow}(\epsilon_p, \dot{\epsilon}, T) = (1 - F)\sigma^m(\epsilon_p, \dot{\epsilon}, T) + F\sigma^t(\epsilon_p, \dot{\epsilon}, T), \quad (4)$$

where F is the twin volume fraction, σ^m and σ^t are the flow stresses of the matrix and twin, respectively. The flow stress of the matrix is decomposed into a solution strengthening stress $\sigma_{ss}^m(\dot{\epsilon}, T)$, a grain boundary strengthening stress σ_{HP}^m , and a dislocation forest strengthening stress $\sigma_{for}^m(\epsilon_p, \dot{\epsilon}, T)$. Similarly, the flow stress of the matrix is decomposed into a twin critical stress σ_{crit}^t , a twin boundary strengthening stress σ_{HP}^t , and the effect of the twin on the surrounding dislocation slip $\sigma_{slip}^t(\epsilon_p, \dot{\epsilon}, T)$ [41,65,66]. This is written as

$$\sigma_{flow}(\epsilon_p, \dot{\epsilon}, T) = (1 - F)\left(\sigma_{ss}^m(\dot{\epsilon}, T) + \sigma_{HP}^m + \sigma_{for}^m(\epsilon_p, \dot{\epsilon}, T)\right) + F\left(\sigma_{crit}^t + \sigma_{HP}^t + \sigma_{slip}^t(\epsilon_p, \dot{\epsilon}, T)\right). \quad (5)$$

In this work, the solution strengthening stress of the matrix $\sigma_{ss}^m(\dot{\epsilon}, T)$ is determined by the yield strength obtained from the experiment. The effect of the Hall-Petch term is introduced to describe the grain boundary strengthening stress of the matrix and twins, given respectively as

$$\sigma_{HP}^m = \frac{HP}{\sqrt{d_g}}, \quad (6)$$

$$\sigma_{HP}^t = \frac{HP_t}{\sqrt{d_{twin}}}, \quad (7)$$

where HP is the Hall-Petch coefficient of CrMnFeCoNi HEA (reported value 490 MPa· $\mu\text{m}^{1/2}$ [67]), d_g is the grain size (6.83 μm in this work), and HP_t is the Hall-Petch coefficient of twins. However, this latter parameter is mostly empirically determined in the references and, in this work, its value corresponding to the magnitude of HP . Therefore, it was assumed that $HP_t = HP$. The parameter d_{twin} is the equivalent grain size of a grain containing twins, given as

$$d_{twin} = \frac{1 - F}{\sin(\alpha)n} d_g, \quad (8)$$

where α is the angle between the slip plane and the twins plane, and n is determined by the average number of lamellae inside the matrix grains [66]. The Taylor hardening model describes the dislocation forest strengthening of the matrix, such that

$$\sigma_{for}^m(\epsilon_p, \dot{\epsilon}, T) = M\chi Gb\sqrt{\rho(\epsilon_p, \dot{\epsilon}, T)}, \quad (9)$$

where M is the Taylor constant, χ is the dislocation hardening coefficient, G is the shear modulus, and $\rho(\epsilon_p, \dot{\epsilon}, T)$ is the dislocation density. The evolution of the dislocation density is described by the Kocks-Mecking-Estrin evolution law model [68], given as

$$\frac{d\rho}{d\epsilon_p} = M\left(\frac{1}{bL} - f(\dot{\epsilon}, T)\rho\right), \quad (10)$$

where $f(\dot{\epsilon}, T)$ is the strain rate and temperature-dependent dynamic recovery coefficient of dislocation, and L is the mean free path expressed by

$$\frac{1}{L} = \frac{1}{d_g} + k\sqrt{\rho}, \quad (11)$$

where k is the work hardening coefficient. Additionally, $\sigma_{slip}^t(\epsilon_p, \dot{\epsilon}, T)$ increases in proportion to the slip dislocation density such that

$$\sigma_{slip}^t(\epsilon_p, \dot{\epsilon}, T) = MGCbb_t\rho(\epsilon_p, \dot{\epsilon}, T), \quad (12)$$

where C is the twin hardening coefficient, and b_t is the Burgers vector of the twinning dislocation. The evolution of the twin volume fraction F is described as

$$\begin{cases} F = 0 & \sigma_{flow} < \sigma_{crit}^t \\ \frac{dF}{d\epsilon_p} = (1 - F)NV_{tw}\sigma_{flow} \geq \sigma_{crit}^t & \end{cases}, \quad (13)$$

where N is the number of nuclei per unit volume, and the V_{tw} is the volume of a newly-formed twin [69]. In this model, the probability of twin nucleation is related to the current flow stress, given as

$$N = N_0 \exp\left[-\left(\frac{\sigma_{crit}^t}{\sigma_{flow}}\right)^{s(\dot{\epsilon}, T)}\right], \quad (14)$$

where N_0 is the material constant, and $s(\dot{\epsilon}, T)$ is the twin growth efficiency dependent on strain rate and temperature. Among them, The twin critical stress σ_{crit}^t of the CrMnFeCoNi HEA is calculated according to [69, 70]

$$\sigma_{crit}^t = 6.14 \frac{\gamma_{SF}}{b}, \quad (15)$$

where γ_{SF} is the SF energy of the CrMnFeCoNi HEA, and its value is 30 mJ/m² [71]. In this work, the calculation result of the twin critical stress σ_{crit}^t is 722 MPa. This value is close to those reported by Li et al. and Gludovatz et al. [29,57]. Following twin nucleation, it is assumed that the twin nuclei immediately grow into disc-shaped twins whose diameter and thickness are approximately equal to the grain size and the average twin width, respectively:

$$V_{tw} = \frac{1}{4}\pi e d_g^2, \quad (16)$$

where e is the average twin width. In this work, the value of e is estimated to be 10 nm based on accumulated experimental observations. To summarize, the CrMnFeCoNi HEA constitutive model parameters that exhibit dependence on the evolution of the dislocation density and the twin volume fraction are tabulated in Table 1. We acquired only two experimental data sets of the strain rates, and all experiments in this work were at room temperature. The strain rate-dependent parameters of the constitutive model under the two strain rates are directly given in Table 1, and the temperature dependence of the parameters is not considered in this paper. The evolution models of the dislocation density and twin volume fraction were fitted based on the EBSD experimental data in Section 3.3. Fig. 11(a) shows that the constitutive model with the determined parameters is in excellent agreement with the CrMnFeCoNi HEA tensile test data in this work. Moreover, Figs. 11(b) and 11(c) also indicate that the fitting results of the dislocation density and twin volume fraction evolution models are acceptable.

This constitutive model describes the evolution process of the flow stress in the CrMnFeCoNi HEA. First of all, the dynamic tensile

Table 1

All the parameters of the constitutive model.

	Description	Value
HP	Hall-Petch coefficient	490 MPa· $\mu\text{m}^{1/2}$
d_g	average grain size	6.83 μm
α	angle between the slip plane and the twin plane	60°
n	average number of twin lamellae inside grains	5
M	Taylor constant	3.06
χ	dislocation hardening coefficient	0.47 *
G	shear modulus	79.3 GPa
b	Burgers vector	2.55 nm
$f(Q)$	dislocation dynamic recovery coefficient ($5 \times 10^{-4} \text{ s}^{-1}$)	2.08 **
$f(D)$	dislocation dynamic recovery coefficient (7000 s^{-1})	1.66 **
k	work hardening coefficient	0.012 *
C	twin hardening coefficient	1900 *
b_t	Burgers vector of twinning dislocation	1.04 nm
N_0	materials constant	$2.3\text{E}+17$ *
$s(Q)$	twin growth efficiency ($5 \times 10^{-4} \text{ s}^{-1}$)	0.89 **
$s(D)$	twin growth efficiency (7000 s^{-1})	1 **
γ_{SF}	stacking fault (SF) energy	30 mJ/m ²
E	average twin width	10 nm

* fitted strain rate-independent parameter.

** fitted strain rate-dependent parameter.

specimens exhibit a higher yield strength than the quasi-static tensile specimens. The low dislocation dynamic recovery coefficient under dynamic tension indicates that the dislocation density of the material increases rapidly. Additionally, the higher dislocation density in the dynamic tensile specimen causes the flow stress to reach the twin critical stress earlier, at a strain of 0.08. However, the flow stress of the quasi-static specimen satisfies the stress condition of twin nucleation at the strain of 0.12. After twin nucleation, the twin evolution rate of the quasi-static tensile specimens is limited, whereas the dynamic tensile specimens possess a higher twin growth efficiency toward twin nucleation

and multiplication. Specifically, the twin volume fraction of the final dynamic tensile specimens is 6.1 times higher than that of the quasi-static tensile specimens. In conclusion, the flow stress enhancement of the CrMnFeCoNi HEA under dynamic tension is owing to its high dislocation density and a certain scale of twins. To describe the contribution of the matrix and twins to the flow stress of the studied CrMnFeCoNi HEA, Fig. 12 shows area graphs of the matrix and twins in the flow stress of the quasi-static and dynamic tensile specimens. The effect of twinning strengthening is feeble in the quasi-static tensile specimens, and dislocation forest strengthening plays the dominant role in the quasi-static flow stress strengthening of the studied alloys. Correspondingly, twins in the dynamic tensile specimens provide 27% of the work hardening. This result indicates that twins make an essential contribution to enhancing the dynamic flow stress of the studied alloys.

5. Conclusion

The strain rate-dependent mechanical behaviors of the CrMnFeCoNi HEA were studied using quasi-static and dynamic tensile experiments. The accuracy of the dynamic experiment was verified using high-speed photography and DIC calculation. The multiscale microstructural evolution of the deformed specimens was observed and analyzed with a series of SEM, EBSD, and TEM experiments. On the basis of these experimental results, a thermo-viscoplastic constitutive model was established to describe the mechanical behavior of the CrMnFeCoNi HEA under dynamic tension by taking into account the enhancement of alloy strength via the presence of twins. The influence that the microstructural evolution has on the deformation behavior of the alloys was discussed. The key conclusions are summarized below:

- (1) The studied CrMnFeCoNi HEA possessed an excellent strength-plasticity combination under dynamic tension. The yield stress,

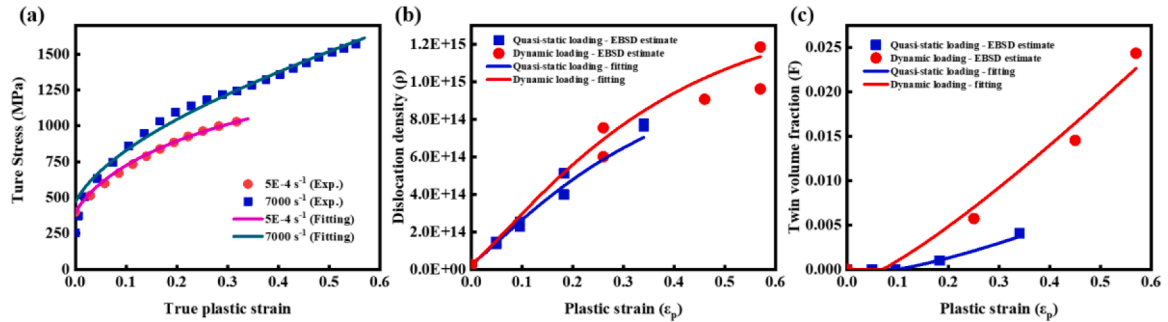


Fig. 11. (a) The flow stress of the quasi-static ($5 \times 10^{-4} \text{ s}^{-1}$) and dynamic (7000 s^{-1}) tensile tests (data points) and the accurate fitting results of the constitutive model in this work (solid lines); (b) dislocation density calculated by KAM maps (data points) and fitted dislocation density evolution curves (solid lines); (c) twin volume fraction calculated by EBSD results (data points) and fitted evolution curves (solid lines).

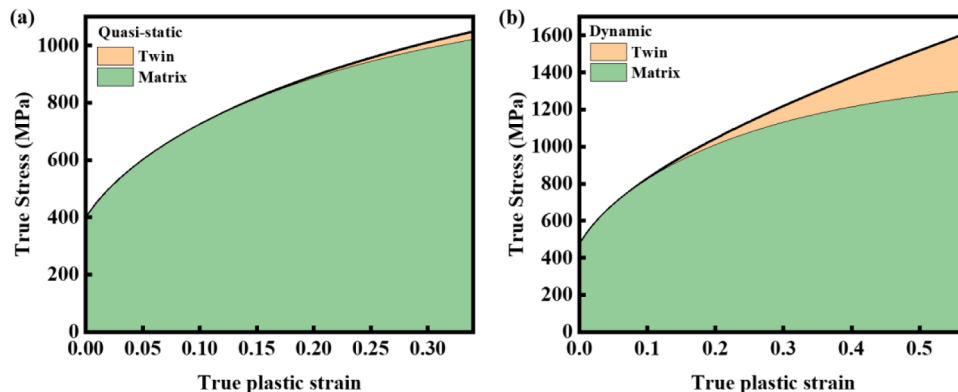


Fig. 12. Area graphs of the proportion of the matrix and twins in the flow stress of the (a) quasi-static and (b) dynamic tensile specimens.

true ultimate stress, and strain of the alloys under dynamic tensile loading increased by 18%, 52%, and 68% to 472 MPa, 1586 MPa, and 0.57, respectively, in comparison to the yield stress (399 MPa), true ultimate stress (1042 MPa), and strain (0.34) under quasi-static tension.

- (2) The high-speed photographic observation showed that the deformation of the sample was uniform and there was no premature strain localization. Furthermore, the fracture morphologies of the specimens under the two loading conditions were significantly different. The quasi-static tensile specimen fractures were the common plastic dimple fracture. In contrast, the fracture surface of the dynamic tensile specimens manifested the limited brittle transition and consisted of dimples and quasi-cleavage fractures.
- (3) Under dynamic tensile loading, the dislocation density of the specimen, as calculated by KAM maps, was higher and the dislocation cell size was smaller than that under quasi-static tensile loading. This result signified that the dislocation evolution was more active under dynamic tension. Furthermore, few twins existed in the quasi-static tensile specimens, whereas ample thin and dense twin lamellas were commonly observed in the dynamic tensile specimens. The twin statistics results revealed that the twin volume fraction of the dynamic tensile specimens was about six times that of the quasi-static tensile specimens. The interaction between the dislocations and the efficiently-evolved twins has the ability to accommodate considerable plastic strain. Thus, the plasticity of the alloys is enhanced under dynamic tension.
- (4) The fitting results of the constitutive model, based on the evolution of the dislocation density and twin volume fraction, agreed with the experimental results herein. These constitutive model results indicated that the strength enhancement of the alloys under dynamic tension is primarily provided by dislocation forest hardening accompanying high dislocation density and strong dislocation motion resistance from twins.

CRedit authorship contribution statement

Yu Qiao: Writing – original draft, Writing – review & editing, Investigation, Formal analysis. **Yan Chen:** Supervision, Formal analysis, Writing – review & editing. **Fu-Hua Cao:** Writing – review & editing. **Hai-Ying Wang:** Formal analysis. **Lan-Hong Dai:** Conceptualization, Supervision, Formal analysis, Writing – review & editing.

Declaration of Competing Interest

The authors declare that they have no known competing financial interests or personal relationships that could have appeared to influence the work reported in this paper.

Acknowledgment

This research was supported by the National Key Research and Development Program of China (No. 2017YFB0702003), the NSFC (Nos. 11790292, 11972346 and 11672316), the NSFC Basic Science Center Program for “Multiscale Problems in Nonlinear Mechanics” (No.11988102), the Strategic Priority Research Program of the Chinese Academy of Sciences (Nos. XDB22040302 and XDB22040303), the Key Research Program of Frontier Sciences of the Chinese Academy of Sciences (No. QYZDJSSW-JSC011), and the Science Challenge Project (No. TZ2018001).

References

- [1] Yu T, Zhang L. Plastic bending: theory and applications. World Scientific; 1996.
- [2] Lu G, Yu T. Energy absorption of structures and materials. Elsevier; 2003.

- [3] Meyers MA. Dynamic behavior of materials. John Wiley & sons; 1994.
- [4] Stronge WJ, Yu T. Dynamic models for structural plasticity. Springer Science & Business Media; 2012.
- [5] Sonstabo JK, Morin D, Langseth M. Static and dynamic testing and modelling of aluminium joints with flow-drill screw connections. *Int J Impact Eng* 2018;115: 58–75.
- [6] Zhu J, Xia Y, Zhou Q, Wierzbicki T. A rate-dependent model for metals based on a master curve of normalized hardening behavior of DP steels. *J Dyn Behav Mater* 2016;2(2):272–82.
- [7] Li Q, Meng H. About the dynamic strength enhancement of concrete-like materials in a split Hopkinson pressure bar test. *Int J Solids Struct* 2003;40(2):343–60.
- [8] Wen K, Chen X-W, Chi R-Q, Lu Y-G. Analysis on the fragmentation pattern of sphere hypervelocity impacting on thin plate. *Int J Impact Eng* 2020;146.
- [9] Tan M, Zhang X, Bao K, Wu Y, Xue W. Interface defeat of ceramic armor. *Adv Mech* 2019;49(1):201905 (In Chinese).
- [10] Jiao W, Chen X. Review on long-rod penetration at hypervelocity. *Adv Mech* 2019; 49(1):201904 (In Chinese).
- [11] Wen K, Chen X-W. Failure evolution in hypervelocity impact of Al spheres onto thin Al plates. *Int J Impact Eng* 2021;147.
- [12] Riedel W, Wicklein M, Thoma K. Shock properties of conventional and high strength concrete: experimental and mesomechanical analysis. *Int J Impact Eng* 2008;35(3):155–71.
- [13] Xu Z, Li Y. Dynamic behaviors of 0Cr18Ni10Ti stainless steel welded joints at elevated temperatures and high strain rates. *Mech Mater* 2009;41(2):121–30.
- [14] Guo YB, Gao GF, Jing L, Shim VPW. Response of high-strength concrete to dynamic compressive loading. *Int J Impact Eng* 2017;108:114–35.
- [15] Zhao H, Elnasri I, Abdennadher S. An experimental study on the behaviour under impact loading of metallic cellular materials. *Int J Mech Sci* 2005;47(4-5):757–74.
- [16] Liu F, Li QM. Strain-rate effect on the compressive strength of brittle materials and its implementation into material strength model. *Int J Impact Eng* 2019;130: 113–23.
- [17] Zhang W, Yin S, Yu TX, Xu J. Crushing resistance and energy absorption of pomelo peel inspired hierarchical honeycomb. *Int J Impact Eng* 2019;125:163–72.
- [18] Hong W, Fan H, Xia Z, Jin F, Zhou Q, Fang D. Axial crushing behaviors of multi-cell tubes with triangular lattices. *Int J Impact Eng* 2014;63:106–17.
- [19] Zhang J, Lu G. Dynamic tensile behaviour of re-entrant honeycombs. *Int J Impact Eng* 2020;139.
- [20] Xiao R, Hou B, Sun QP, Zhao H, Li YL. An experimental investigation of the nucleation and the propagation of NiTi martensitic transformation front under impact loading. *Int J Impact Eng* 2020;140.
- [21] Chang B, Zheng Z, Zhang Y, Zhao K, He S, Yu J. Crashworthiness design of graded cellular materials: An asymptotic solution considering loading rate sensitivity. *Int J Impact Eng* 2020;143.
- [22] George EP, Raabe D, Ritchie RO. High-entropy alloys. *Nat Rev Mater* 2019;4(8): 515–34.
- [23] George EP, Curtin WA, Tasan CC. High entropy alloys: a focused review of mechanical properties and deformation mechanisms. *Acta Mater* 2020;188: 435–74.
- [24] Ma E. Unusual dislocation behavior in high-entropy alloys. *Scr Mater* 2020;181: 127–33.
- [25] Li Z, Zhao S, Ritchie RO, Meyers MA. Mechanical properties of high-entropy alloys with emphasis on face-centered cubic alloys. *Prog Mater Sci* 2019;102:296–345.
- [26] Yeh JW, Chen SK, Lin SJ, Gan JY, Chin TS, Shun TT, Tsau CH, Chang SY. Nanostructured high-entropy alloys with multiple principal elements: novel alloy design concepts and outcomes. *Adv Eng Mater* 2004;6(5):299–303.
- [27] Cantor B, Chang ITH, Knight P, Vincent AJB. Microstructural development in equiatomic multicomponent alloys. *Mater Sci Eng* 2004;375-377:213–8.
- [28] Zhang Y, Zuo TT, Tang Z, Gao MC, Dahmen KA, Liaw PK, Lu ZP. Microstructures and properties of high-entropy alloys. *Prog Mater Sci* 2014;61:1–93.
- [29] Gludovatz B, Hohenwarter A, Catoor D, Chang EH, George EP, Ritchie R. A fracture-resistant high-entropy alloy for cryogenic applications. *Science* 2014; 345(6201):1153–8.
- [30] Laplanche G, Kostka A, Horst OM, Eggeler G, George EP. Microstructure evolution and critical stress for twinning in the CrMnFeCoNi high-entropy alloy. *Acta Mater* 2016;118:152–63.
- [31] Liu J-P, Chen J-X, Liu T-W, Li C, Chen Y, Dai L-H. Superior strength-ductility CoCrNi medium-entropy alloy wire. *Scr Mater* 2020;181:19–24.
- [32] Li Z, Zhao S, Diao H, Liaw PK, Meyers MA. High-velocity deformation of Al_{0.3}CoCrFeNi high-entropy alloy: Remarkable resistance to shear failure. *Sci Rep* 2017;7:42742.
- [33] Pu Z, Xie ZC, Sarmah R, Chen Y, Lu C, Ananthakrishna G, Dai LH. Spatio-temporal dynamics of jerky flow in high-entropy alloy at extremely low temperature. *Philos Mag* 2020;1–25.
- [34] Pu Z, Chen Y, Dai LH. Strong resistance to hydrogen embrittlement of high-entropy alloy. *Mater Sci Eng* 2018;736:156–66.
- [35] Liu X-F, Tian Z-L, Zhang X-F, Chen H-H, Liu T-W, Chen Y, Wang Y-J, Dai L-H. Self-sharpening tungsten high-entropy alloy. *Acta Mater* 2020;186:257–66.
- [36] Jiang ZJ, He JY, Wang HY, Zhang HS, Lu ZP, Dai LH. Shock compression response of high entropy alloys. *Mater Res Lett* 2016;4(4):226–32.
- [37] Li Z, Zhao S, Alotaibi SM, Liu Y, Wang B, Meyers MA. Adiabatic shear localization in the CrMnFeCoNi high-entropy alloy. *Acta Mater* 2018;151:424–31.
- [38] Ma Y, Yuan F, Yang M, Jiang P, Ma E, Wu X. Dynamic shear deformation of a CrCoNi medium-entropy alloy with heterogeneous grain structures. *Acta Mater* 2018;148:407–18.

- [39] Wang L, Qiao JW, Ma SG, Jiao ZM, Zhang TW, Chen G, Zhao D, Zhang Y, Wang ZH. Mechanical response and deformation behavior of Al_{0.6}CoCrFeNi high-entropy alloys upon dynamic loading. *Mater Sci Eng* 2018;727:208–13.
- [40] Hu M-I, Song W-d, Duan D-b, Wu Y. Dynamic behavior and microstructure characterization of TaNbHfZrTi high-entropy alloy at a wide range of strain rates and temperatures. *Int J Mech Sci* 2020:182.
- [41] Zhang TW, Ma SG, Zhao D, Wu YC, Zhang Y, Wang ZH, Qiao JW. Simultaneous enhancement of strength and ductility in a NiCoCrFe high-entropy alloy upon dynamic tension: micromechanism and constitutive modeling. *Int J Plast* 2020;124:226–46.
- [42] Cao CM, Tong W, Bukhari SH, Xu J, Hao YX, Gu P, Hao H, Peng LM. Dynamic tensile deformation and microstructural evolution of Al_xCrMnFeCoNi high-entropy alloys. *Mater Sci Eng* 2019;759:648–54.
- [43] He J, Wang Q, Zhang H, Dai L, Mukai T, Wu Y, Liu X, Wang H, Nieh T-G, Lu Z. Dynamic deformation behavior of a face-centered cubic FeCoNiCrMn high-entropy alloy. *Sci Bull* 2018;63(6):362–8.
- [44] Zhang S, Wang Z, Yang HJ, Qiao JW, Wang ZH, Wu YC. Ultra-high strain-rate strengthening in ductile refractory high entropy alloys upon dynamic loading. *Intermetallics* 2020:121.
- [45] Gao TJ, Zhao D, Zhang TW, Jin T, Ma SG, Wang ZH. Strain-rate-sensitive mechanical response, twinning, and texture features of NiCoCrFe high-entropy alloy: Experiments, multi-level crystal plasticity and artificial neural networks modeling. *J Alloys Compd* 2020;845.
- [46] Yang Z, Yang M, Ma Y, Zhou L, Cheng W, Yuan F, Wu X. Strain rate dependent shear localization and deformation mechanisms in the CrMnFeCoNi high-entropy alloy with various microstructures. *Mater Sci Eng* 2020:793.
- [47] Han Z, Ren W, Yang J, Du Y, Wei R, Zhang C, Chen Y, Zhang G. The deformation behavior and strain rate sensitivity of ultra-fine grained CoNiFeCrMn high-entropy alloys at temperatures ranging from 77 K to 573 K. *J Alloys Compd* 2019;791:962–70.
- [48] Xiao Y, Kozak R, Haché MJR, Steurer W, Spolenak R, Wheeler JM, Zou Y. Micro-compression studies of face-centered cubic and body-centered cubic high-entropy alloys: size-dependent strength, strain rate sensitivity, and activation volumes. *Mater Sci Eng* 2020:790.
- [49] Chen S, Xie X, Li W, Feng R, Chen B, Qiao J, Ren Y, Zhang Y, Dahmen KA, Liaw PK. Temperature effects on the serrated behavior of an Al_{0.5}CoCrCuFeNi high-entropy alloy. *Mater Chem Phys* 2018;210:20–8.
- [50] Song B, Chen WW, Lu WY. Mechanical characterization at intermediate strain rates for rate effects on an epoxy syntactic foam. *Int J Mech Sci* 2007;49(12):1336–43.
- [51] Cheng Y, Liu J, Pan J, Meng L, Wang H, Mao H, Yang J. Experiment method of deriving the dynamic mechanical parameters of metal materials. *China Measur Test* 2016;42:107–12 (in Chinese).
- [52] Hasnaoui A, Van Swygenhoven H, Derlet PM. Dimples on nanocrystalline fracture surfaces as evidence for shear plane formation. *Science* 2003;300:1550–2.
- [53] Martin ML, Fenske JA, Liu GS, Sofronis P, Robertson IM. On the formation and nature of quasi-cleavage fracture surfaces in hydrogen embrittled steels. *Acta Mater* 2011;59(4):1601–6.
- [54] Courtas S, Grégoire M, Federspiel X, Bicaïs-Lepinay N, Wyon C. Electron backscattered diffraction (EBSD) use and applications in newest technologies development. *Microelectron Reliab* 2006;46(9-11):1530–5.
- [55] Zribi Z, Ktari HH, Herbst F, Optasanu V, Njah NE. XRD and SRS characterization of a casting Al-7wt%Si alloy processed by equal channel angular extrusion: dislocation density evaluation. *Mater Charact* 2019;153:190–8.
- [56] Ateba Betanda Y, Helbert A-L, Brisset F, Mathon M-H, Waeckerlé T, Baudin T. Measurement of stored energy in Fe-48%Ni alloys strongly cold-rolled using three approaches: Neutron diffraction, Dillamore and KAM approaches. *Mater Sci Eng* 2014;614:193–8.
- [57] Li J, Yi M, Wu H, Fang Q, Liu Y, Liu B, Zhou K, Liaw PK. Fine-grain-embedded dislocation-cell structures for high strength and ductility in additively manufactured steels. *Mater Sci Eng* 2020:790.
- [58] Galindo-Nava EI, Rivera-Díaz-del-Castillo PEJ. A thermodynamic theory for dislocation cell formation and misorientation in metals. *Acta Mater* 2012;60(11):4370–8.
- [59] Noronha SJ, Farkas D. Effect of dislocation blocking on fracture behavior of Al and α -Fe: a multiscale study. *Mater Sci Eng* 2004;365(1-2):156–65.
- [60] He BB, Hu B, Yen HW, Cheng GJ, Wang ZK, Luo HW, Huang MX. High dislocation density-induced large ductility in deformed and partitioned steels. *Science* 2017;357:1029–32.
- [61] He F, Wang Z, Wu Q, Chen D, Yang T, Li J, Wang J, Liu CT, Kai J-j. Tuning the defects in face centered cubic high entropy alloy via temperature-dependent stacking fault energy. *Scr Mater* 2018;155:134–8.
- [62] Jin ZH, Gumbsch P, Albe K, Ma E, Lu K, Gleiter H, Hahn H. Interactions between non-screw lattice dislocations and coherent twin boundaries in face-centered cubic metals. *Acta Mater* 2008;56(5):1126–35.
- [63] Lu K, Lu L, Suresh SJ. Strengthening materials by engineering coherent internal boundaries at the nanoscale. *Science* 2009;324(5925):349–52.
- [64] Lu L, Chen X, Huang X, Lu KJS. Revealing the maximum strength in nanotwinned copper. *Science* 2009;323(5914):607–10.
- [65] Beyerlein LJ, Tomé CN. A dislocation-based constitutive law for pure Zr including temperature effects. *Int J Plast* 2008;24(5):867–95.
- [66] Zecevic M, Knezevic M, Beyerlein LJ, Tomé CN. An elasto-plastic self-consistent model with hardening based on dislocation density, twinning and de-twinning: application to strain path changes in HCP metals. *Mater Sci Eng* 2015;638:262–74.
- [67] Sun SJ, Tian YZ, Lin HR, Dong XG, Wang YH, Zhang ZJ, Zhang ZF. Enhanced strength and ductility of bulk CoCrFeMnNi high entropy alloy having fully recrystallized ultrafine-grained structure. *Mater Des* 2017;133:122–7.
- [68] Bouaziz O, Estrin Y, Bréchet Y, Embury JD. Critical grain size for dislocation storage and consequences for strain hardening of nanocrystalline materials. *Scr Mater* 2010;63(5):477–9.
- [69] Liang ZY, Wang X, Huang W, Huang MX. Strain rate sensitivity and evolution of dislocations and twins in a twinning-induced plasticity steel. *Acta Mater* 2015;88:170–9.
- [70] Byun TS. On the stress dependence of partial dislocation separation and deformation microstructure in austenitic stainless steels. *Acta Mater* 2003;51(11):3063–71.
- [71] Okamoto NL, Fujimoto S, Kambara Y, Kawamura M, Chen ZM, Matsunoshita H, Tanaka K, Inui H, George EP. Size effect, critical resolved shear stress, stacking fault energy, and solid solution strengthening in the CrMnFeCoNi high-entropy alloy. *Sci Rep* 2016;6:35863.